

Femtosecond dynamics of electronic states in the Mott insulator 1T-TaS₂ by time resolved photoelectron spectroscopy

L Perfetti^{1,4}, P A Loukakos¹, M Lisowski¹,
U Bovensiepen¹, M Wolf¹, H Berger²,
S Biermann³ and A Georges³

¹ Fachbereich Physik, Freie Universität Berlin, Arnimallee 14,
14195 Berlin, Germany

² Institut de Physique de la Matière Complexe, EPFL,
CH-1015 Lausanne, Switzerland

³ Centre de Physique Theorique, École Polytechnique,
91128 Palaiseau Cedex, France

E-mail: perfetti@physik.fu-berlin.de

New Journal of Physics **10** (2008) 053019 (17pp)

Received 13 March 2008

Published 14 May 2008

Online at <http://www.njp.org/>

doi:10.1088/1367-2630/10/5/053019

Abstract. Photoexcitation of the Mott insulator 1T-TaS₂ by an intense laser pulse leads to an ultrafast transition toward a gapless phase. Besides the collapse of the electronic gap, the sudden excitation of the charge density wave (CDW) mode results in periodic oscillations of the electronic states. We employ time resolved photoelectron spectroscopy to monitor the rich dynamics of electrons and phonons during the relaxation toward equilibrium. The qualitative difference between the oscillatory dynamics of the CDW and the monotonic recovery of the electronic gap proves that 1T-TaS₂ is indeed a Mott insulator. Moreover the quasi-instantaneous build-up of mid gap states is in contrast with the retarded response expected from a Peierls insulating phase. Interestingly, the photoinduced electronic states in the midgap spectral region display a weak resonance that is reminiscent of a quasiparticle peak.

⁴ Author to whom any correspondence should be addressed.

Contents

1. Introduction	2
2. Material and methods	4
2.1. Experimental set-up	4
2.2. Structural and electronic properties of 1T-TaS ₂	5
2.3. Analysis of time-resolved photoelectron measurements	6
3. Results and discussion	7
3.1. Dynamics of electrons after photoexcitation of the metal	7
3.2. Dynamics and spectroscopy of the photoexcited insulator	9
4. Theoretical modeling	14
5. Conclusions	15
Acknowledgments	16
References	16

1. Introduction

During the early development of solid state theory, most materials were classified as metals or insulators from the filling of their electronic band structure. However, several oxides that were expected to be metallic did not fulfill this theoretical prediction. In 1937 Mott and Peierls [1] proposed that compounds with a half filled conduction band can be electrical insulators if the Coulomb repulsion between electrons is large enough to drive a localization of the charge carriers. Since then, many experimental and theoretical efforts have contributed to the understanding of the transition to the Mott insulating (MI) phase [2, 3].

Although the localization of electrons in a Mott phase is purely driven by electron–electron (e–e) interaction, a realistic description of highly correlated materials should also account for the coupling of electrons to the nuclear lattice. Indeed, the electron–phonon (e–ph) coupling may induce a charge ordering that competes or coexists with the Mott insulator. For this reason, several MI compounds display an insulator–metal transition at the critical temperature of a lattice instability [2]. If the e–ph coupling originates from few lattice modes, the lattice instability takes place via phonon softening [4]. The resulting distortion of the nuclear structure comes along with a modulation of the charge density referred to as the charge density wave (CDW). The CDW favors a MI instability when the lattice distortion reduces the bandwidth and preserves an odd filling of the conducting band. This case has been proposed to explain the metal–insulator transition of 1T-TaS₂ [5] and at the surface of 1T-TaSe₂ [6, 7]. According to this scenario, a lattice instability increases the CDW amplitude, leading to a reduction of the electronic bandwidth below the critical value for a Mott transition. Following experiments proved that photoemission spectra of 1T-TaSe₂ are consistent with the Hubbard model for suitable choice of the Coulomb repulsion U and the electronic bandwidth W [6]. In the language of the Hubbard model—see the phase diagram, figure 1—we identify the MI phase and metallic phase of 1T-TaS₂ with $U = 1.4W$ and $U < 1.2W$, respectively.

Despite the success of the Hubbard model to describe the Mott transition in this compound, a complete understanding of the interplay between the CDW and the MI phase requires effects due to e–e correlations and e–ph coupling to be distinguished. This is possible only for out of equilibrium conditions, namely by monitoring the response of the correlated material to an

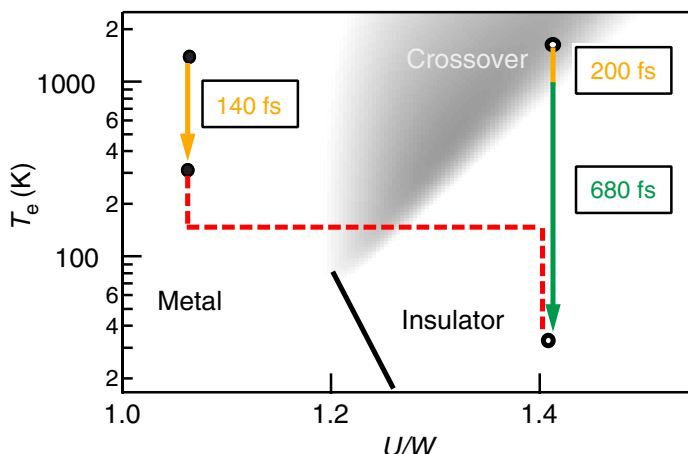


Figure 1. Phase diagram of the half filled Hubbard model as a function of the electronic temperature T_e . The bottom axis plots the Coulomb repulsion $U = 0.5$ eV divided by the electronic bandwidth W . A smooth crossover connects the metallic phase with the insulating phase at high electronic temperature. When T_e is equal to the lattice temperature T_l (equilibrium conditions), the metal–insulator transition of 1T-TaS₂ (red dashed line) is due to an abrupt reduction of the electronic bandwidth at $T_l = T_e = 150$ K. Photoexcitation by an optical pump pulse induces a large increase of T_e without significant changes of T_l and W . The cooling of hot electrons displays different dynamics if the system is originally in the metallic phase (yellow arrow) or in the MI phase (yellow-green arrow).

ultrafast optical perturbation. As shown in figure 2, the scattering processes due to e–e and e–ph interactions take place on quite different timescales. It follows that laser pulses with duration of 10–100 fs have a bandwidth small enough to investigate the electronic states in the ‘energy domain’, while monitoring the coupling of these states to the lattice in the ‘time domain’. Moreover, the ‘incoherent’ emission and ‘coherent’ excitation of phonons follow two distinct temporal evolutions. For example, the monotonic transfer of electronic energy to the lattice [8] is qualitatively different from the periodic oscillation of impulsively excited phonon modes [9]. For this reason, optical pump–probe spectroscopy is often employed to investigate photoinduced transitions in correlated materials [10]–[14]. The combination of ultrafast laser sources with angular resolved photoelectron spectroscopy (ARPES) is especially powerful since time-resolved ARPES directly monitors the temporal evolution of electronic states. Thereby, an intense pulse in the infrared spectral range promotes the system into a highly excited state, whereas an ultraviolet probe pulse emits photoelectrons after a variable time delay [15]–[17].

Time-resolved ARPES has been recently exploited to investigate the coexisting CDW and MI phases in 1T-TaS₂ [18]. The results can be summarized as follows: upon absorption of the pump pulse the electronic temperature T_e increases abruptly while the lattice temperature T_l and the electronic bandwidth are almost unchanged. This process initiates a photoinduced crossover from the Mott insulator to a gapless phase. Besides, the electronic states display periodic modulations of the binding energy due to the ultrafast excitation of the CDW amplitude mode.

In this paper, we show that photoexcited electrons display qualitatively different dynamics depending whether 1T-TaS₂ is originally in the metallic or MI phase. In the metallic phase,

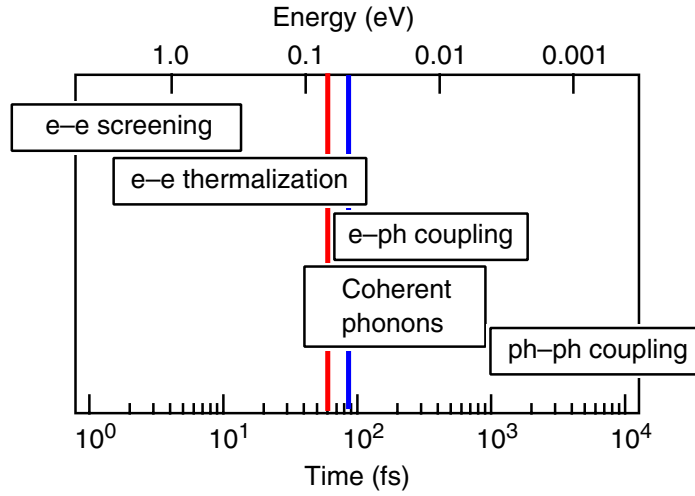


Figure 2. Typical timescales (bottom axis) and energy scales (top axis) of coherent phonons, e–e interaction, e–ph interaction and ph–ph interaction in correlated metals. The red and blue line indicate the temporal duration of our pump pulse and probe pulse, respectively.

the electronic temperature follows a single exponential decay of 140 fs (yellow arrow in figure 1) and is approximately described by the two temperature model. The spectral weight near to the Fermi level shows weak oscillations due to the coherent displacement of the CDW amplitude mode. This coherent phonon decays by electron–hole pair formation with a damping time comparable to the oscillation period. Below the transition temperature $T_1 = T_c < 150$ K, the 1T-TaS₂ is a Mott insulator. The density of the states vanishes at the Fermi level, while the missing spectral weight is transferred to the lower and upper Hubbard bands (LHB and UHB). Upon photoexcitation of the MI phase, the electronic gap is filled by electronic states with a peak near to the chemical potential. Such midgap resonance is typical of a Fermi liquid and suggests the presence of quasi-particle states. The relaxation of the photoexcited insulator displays anomalous dynamics. Hot electrons dissipate energy with a faster and slower timescale of 200 and 680 fs, respectively (yellow-green arrow in figure 1). Moreover, the oscillation of the CDW mode has a damping time one order of magnitude longer than in the metallic phase.

2. Material and methods

2.1. Experimental set-up

Time-resolved ARPES combines femtosecond laser system with the photoemission technique [16]: a regenerative Ti:sapphire amplifier provides pulses with center photon energy of 1.5 eV ($\simeq 830$ nm), duration of 50 fs and repetition rate of 200 KHz. Part of the amplifier output is frequency doubled in a β -BaB₂O₄ (BBO) crystal and compressed by prisms. The resulting 3 eV beam is focused on a second BBO crystal in order to generate 6 eV pulses. After traveling through a second prism compressor, these ultraviolet pulses have durations of 80 fs. Both the 1.5 and 6 eV beams are focused on the sample almost collinearly, with focal diameter of 200 and 80 μ m, respectively. If not explicitly stated, the data refer to an absorbed pump fluence of $\phi = 135 \mu\text{J cm}^{-2}$. A delay stage varies the optical path of the 6 eV probe pulse with respect

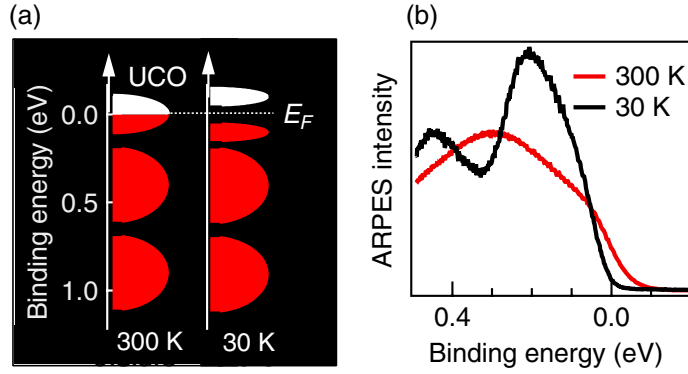


Figure 3. (a) Sketch of the Ta d-like electronic states in the CDW phase. The uppermost subband of the metallic phase ($T_1 = 300$ K) splits into two Hubbard bands in the Mott phase ($T_1 = 30$ K). Normal emission spectra acquired at room temperature (red curve) and $T_1 = 30$ K (black curve).

to the 1.5 eV pump pulse. Both beams propagate with an incident angle of 45° with respect to the surface normal and are p-polarized with respect to the plane of incidence.

Single crystals of 1T-TaS₂ were grown from high purity tantalum wire and vacuum resublimated sulfur by the iodine transport method [19]. The samples were mounted on a cryogenic manipulator and were cleaved *in situ* at a base pressure of 10^{-11} mbar. Photoelectrons emitted along the surface normal were detected by a time of flight (TOF) spectrometer with energy resolution of 10 meV and acceptance angle of $\pm 3.5^\circ$. In order to avoid space charging artifacts, the intensity of the 6 eV beam has been reduced until any distortion of the photoelectron spectra is below the energy resolution of the electron spectrometer. Multiphoton photoemission from the 1.5 eV beam is 100 times weaker than the direct photoemission process. We eliminate this small background by collecting a spectrum with the pump beam alone and subtracting it from the pump–probe spectra. The cross correlation between probe and pump pulse (FWHM of 125 fs) is obtained by detecting photoelectrons with kinetic energy of $\simeq 1.5$ eV as a function of the relative delay. These photoelectrons correspond to photohole excitations 1 eV above the Fermi level and have decay time faster than the duration of the laser pulses.

2.2. Structural and electronic properties of 1T-TaS₂

1T-TaS₂ is a transition metal dichalcogenide that consists of strongly bound S–Ta–S layers that are weakly coupled by interplane interaction. Such a layered structure determines a marked anisotropy in the electrical resistivity [20] and the mechanical properties of the material. X-ray scattering [21] and scanning tunneling microscopy (STM) [22] show that 1T-TaS₂ displays a pronounced lattice modulation already at room temperature. The strong coupling between valence electrons and phonons periodically distorts the lattice, modifying the spatial distribution of the charge density [4]. In real space, the local distortion leads to metallic clusters containing 13 Ta atoms each. As shown in figure 3(a), the CDW formation splits the occupied Ta d-like band into three different manifolds [23]–[25]. The uppermost subband is half filled and therefore susceptible to a Mott transition. Upon cooling below $T_1 = 180$ K, the CDW wave locks into a $\sqrt{13} \times \sqrt{13}$ phase. At the same time, the resistivity increases by one order of magnitude [26] due to the collective localization of

the charge carriers. The ARPES spectra of figure 3(b) show that such a metal–insulator transition induces a large transfer of spectral weight from the Fermi level to the LHB and UHB [6, 18, 27]. A large transfer of spectral weight has been observed also by scanning tunneling spectroscopy (STS) [7, 22] and optical conductivity measurements [28, 29]. The latter technique indicates the opening of an electronic gap $\Delta \simeq 0.1$ eV. The metal–insulator transition can be reversed by increasing the temperature above 220 K [26], applying external pressure [30] or doping the compound with 0.5–1% of Ti atoms [5, 26].

The 1T-TaS₂ is an ideal compound to perform time-resolved photoemission. Thanks to the layered crystal structure, this compound cleaves easily and displays good surface quality. The surface layer does not reconstruct and exhibits very similar properties to the bulk [31]. Moreover the quasi-two-dimensional character of the electronic states minimize the spectral broadening due to the finite photoelectron lifetime [32] and the ballistic transport of photoexcited electrons from the surface towards the bulk [16]. Since the work function of the surface is $\Phi = 5.5$ eV, the probe pulses with $h\nu_{4th} = 6$ eV generate photoholes up to the binding energy $\epsilon = h\nu_{4th} - \Phi = 0.5$ eV. The small kinetic energy of the photoelectrons limits the wavevector to the maximum value $k_{\parallel} < 0.36 \text{ \AA}^{-1}$. This boundary condition does not constrain our experiment because we are interested in electronic states near the Fermi level and at the center of the Brillouin zone ($k_{\parallel} \simeq 0$).

2.3. Analysis of time-resolved photoelectron measurements

Several assumptions are necessary to connect the time-resolved photoemission spectra to the dynamics of electronic states. Here, we briefly discuss the main concepts in the framework of many-body theory. Any photoexcited state should be described in terms of a density matrix build out of many-particles states. The optical coherence is retained as long as the density matrix holds non vanishing off-diagonal elements [33]. Due to ultrafast scattering processes among the electrons, the optical coherence of the photoexcited state in highly correlated metals is lost within a few femtoseconds [34]. This process comes along with the build up of screening in the many-particle system. As shown by figure 2, we assume that e–e interactions respond faster than the duration of our pump and probe pulses. Therefore, we describe the electronic states in the energy domain (Lehmann representation of binding ϵ) and the evolution of these states due to coupling with phonon modes in the time domain (as a function of the pump–probe delay τ). Under these conditions, the temporal evolution of single particle excitations is given by the spectral function $A(\epsilon, \tau)$ times the electronic distribution $f(\epsilon, \tau)$.

A second and familiar assumption at the base of our analysis is the sudden approximation. According to the sudden limit, the primary photoelectrons do not suffer any scattering while escaping from the surfaces. Conversely, the secondary photoelectrons scatter strongly, leading to a structureless background in the energy spectrum. ARPES experiments performed with 6 eV on high temperature superconductors support the validity of the sudden approximation even at such low photon energies [35]. The primary photoelectrons with low kinetic energy do not have extrinsic losses. Furthermore, the background of secondary electrons is less pronounced at 6 eV than at deep ultraviolet photon energy (20–50 eV). In the case of 1T-TaS₂, the spectra measured at 6 eV [18] and 21 eV [27] photon energy are very similar. Therefore, we assume that the photoelectron spectrum is proportional to the product $A(\epsilon, \tau) \cdot f(\epsilon, \tau)$. In the following, we define $A_H(\epsilon, \tau)$ and $A_M(\epsilon, \tau)$ as the spectral function of the photoexcited system that is originally in the insulating and metallic phase, respectively.

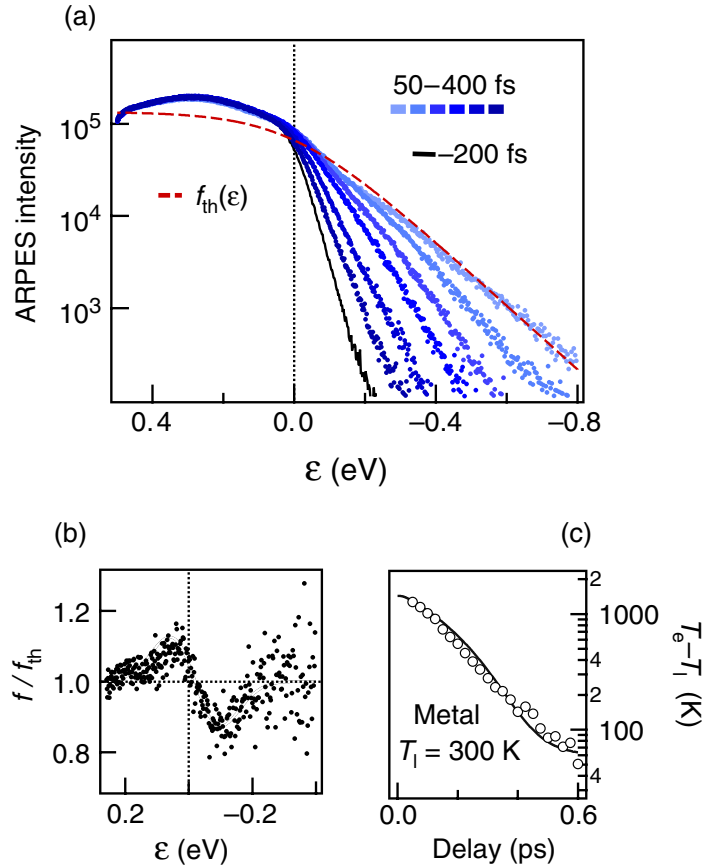


Figure 4. (a) Photoelectron spectrum acquired in the metallic phase ($T_l = 300$ K) at pump–probe delay of 50, 150, 200, 300 and 400 fs (dots) and before the arrival of the pump pulse (black line). The Fermi–Dirac distribution calculated for $T_e = 1500$ K (dashed red line) is superimposed to the spectra. (b) Estimated deviation between the experimental distribution $f(\epsilon, \tau)$ and a Fermi–Dirac distribution $f_{th}(\epsilon, T_e)$ for $\tau = 50$ fs and $T_e = 1500$ K (dots). (c) Difference between electronic temperature and lattice temperature as extracted from the measured spectra (marks) and calculated from the two temperature model (line). The temporal evolution of T_e is well approximated also by a single exponential decay with time constant $\tau_e = 140$ fs.

3. Results and discussion

3.1. Dynamics of electrons after photoexcitation of the metal

We first discuss the electronic dynamics of 1T-TaS₂ in metallic phase at lattice temperature $T_l = 300$ K. The semilogarithmic plot of figure 4(a) displays the time-resolved ARPES spectrum acquired at pump–probe delay $\tau = 50$ fs. The absorption of an 1.5 eV pump pulse with fluence $\phi = 135 \mu\text{J cm}^{-2}$ induces optical transitions between electronic states, exciting about 0.1 electrons of the reconstructed unit cell. The e–e scattering changes the nascent distribution $f(\epsilon, \tau)$ as a function of time, resulting in a Fermi–Dirac distribution $f_{th}(\epsilon, T_e) = (e^{-(\epsilon-\mu)/k_b T_e} + 1)^{-1}$ after thermalization is completed [36]. The electronic temperature T_e is much larger than the

lattice temperature T_l because of the different heat capacities of electrons and phonons. A time-dependent chemical potential $\mu(\tau)$ accounts for the varying density of electronic states in the range $|\epsilon| < 2k_b T_e$. Figure 4(a) displays the photoexcited spectrum at several pump–probe delays and a Fermi–Dirac distribution f_{th} calculated for $T_e = 1500$ K and $\mu = -20$ meV. Notice that f_{th} overlaps well with the tail of the photoelectron spectrum acquired for $\tau = 50$ fs. Indeed, only minor deviations between the experimental f and the calculated f_{th} take place in the proximity of the Fermi level. We estimate the ratio f/f_{th} for $\tau = 50$ fs by: (i) dividing the equilibrium spectrum $A_M \cdot f_{th}$ by a Fermi–Dirac distribution with $T_e = T_l = 300$ K and $\mu = 0$ meV, (ii) extracting from the resulting curve the linear expansion $A_M(\epsilon) = c_0 + c_1\epsilon + O(\epsilon)$, (iii) dividing the photoexcited spectrum $A_M \cdot f$ by $(c_0 + c_1\epsilon) \cdot f_{th}$ with $T_e = 1500$ K and $\mu = -20$ meV. Figure 4(b) shows that f/f_{th} at 50 fs does not exceed 15%, indicating that electrons approach a thermalized distribution within a timescale comparable to the pump pulse duration. This assumption is correct as long as the pump fluence is $\phi > 100 \mu\text{J cm}^{-2}$. At lower excitation density, the longer e–e thermalization questions the definition of an effective $T_e(\tau)$ during cooling of photoexcited electrons.

The delay dependence of the photoelectron spectra in figure 4(a) reflects the temporal evolution of the experimental distribution $f(\tau)$. If we neglect the deviation f/f_{th} , we can estimate $T_e(\tau)$ by fitting f_{th} to the spectra in the energy interval $-0.7 \text{ eV} < \epsilon < -0.1 \text{ eV}$. As shown by figure 4(c), the pump induced increase of electronic temperature decays exponentially with time constant $\tau_e = 140$ fs. Even though T_e reaches 1500 K, the large specific heat of the phonon bath [20] confines the increase of lattice temperature to below 60 K. We neglect ballistic transport of energy from the surface to the bulk [16] because of the strong anisotropy of the layered chalcogenides [20]. In this case, the two temperature model [8] describes the temporal evolution of T_e and T_l via the coupled equations

$$\frac{\partial T_e}{\partial \tau} = -\frac{3\lambda\Omega^2}{\hbar\pi k_B} \frac{T_e - T_l}{T_e} + \frac{P}{C_e}, \quad (1)$$

$$\frac{\partial T_l}{\partial \tau} = \frac{C_e}{C_l} \frac{3\lambda\Omega^2}{\hbar\pi k_B} \frac{T_e - T_l}{T_e}, \quad (2)$$

where C_e and C_l are the electronic- and lattice-specific heat, respectively. The parameter $\lambda\Omega^2$ stands for the second momentum of the Eliashberg coupling function while P is the power delivered by the pump pulse. Within these notations, the dimensionless λ is the average e–ph coupling, while Ω is the mean phonon energy. Figure 4(c) compares the solution of the two temperature model for $\lambda\Omega^2 = 350 \text{ meV}^2$ with the experimental decay of $\Delta T_e = T_e - T_l$. The residual discrepancy is likely due to the approximation of the electronic-specific heat with a linear term of T_e .

Besides a tail of the non-equilibrium distribution, the photoelectron spectra show weak and time-dependent modulations of the intensity. These are largest near the Fermi level, where the CDW displacement more strongly modifies $A_M(\epsilon, \tau)$. Figure 5 displays the intensity map the photoemission intensity and the integrated spectral weight in the energy interval $0 \text{ eV} < \epsilon < 0.1 \text{ eV}$. The signal increases at $\tau = 0$, reaches its maximum for $\tau = 180$ fs and oscillates around a temporal evolving value. We ascribe such dynamics to the ultrafast excitation of the CDW amplitude mode [9]. In real space, this excitation results into the expansion of the Ta clusters toward the undistorted 1T-TaS₂ phase. As a consequence, the release of elastic energy to the electronic system leads to an increase of spectral weight at the Fermi level. Subsequently the

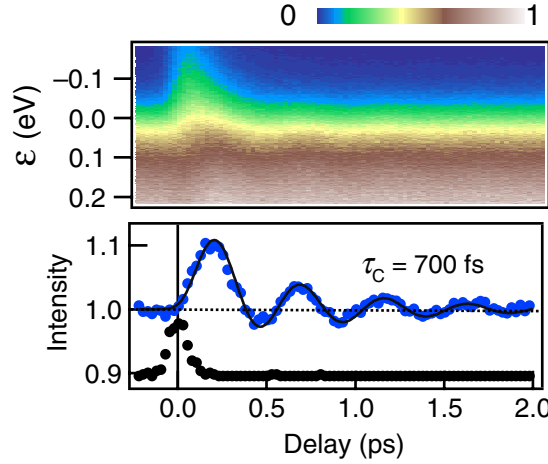


Figure 5. Upper panel: intensity map of the photoelectron counts acquired in the metallic phase ($T_1 = 300$ K). Lower panel: normalized intensity of the photoelectron counts in the energy interval $0 \text{ eV} < \epsilon < 0.1 \text{ eV}$ (blue marks), fit based on equation (3) (black line) and cross-correlation between the pump and probe pulse (black marks).

nuclear structure breathes until a damping force brings the system back to equilibrium. We describe the motion of the phonon coordinate X by the equation

$$\frac{\partial^2 X}{\partial \tau^2} - \frac{\pi}{\tau_C} \frac{\partial X}{\partial \tau} + (2\pi\nu)^2 X = F(\tau), \quad (3)$$

where $F(\tau)$ is the driving force, ν is the phonon frequency and τ_C is the damping time. A calculation of the driving force would require the detailed knowledge of the photoexcitation process, band structure and e-ph coupling [37]. This computational effort is out of the scope of the present paper. Instead, the driving force $F(t)$ is modeled by the step function $\theta(\tau)$ times and exponential decay $e^{-\tau/\tau_F}$. Since F originates from the photoinduced redistribution of electronic charge, the time constant τ_F and electron relaxation time τ_e are expected to be similar. We assume that the modulation of spectral weight is proportional to the convolution of $X(\tau)$ with the cross-correlation between the pump and probe pulse. As shown in figure 5, the result of this calculation reproduces the experimental data well for $\nu = 2.14$ THz, $\tau_C = 700$ fs and $\tau_F = 250$ fs. The central frequency $\nu = 2.14$ THz and short damping time are in agreement with stimulated Raman scattering [38] and transient reflectivity measurements [39]. We attribute the fast damping of the CDW excitation to the strong scattering of the amplitude mode with electron-hole pairs close to the Fermi level. This mechanism is relevant also in semimetals such as graphite and bismuth, leading to a damping time that depends on the density of the electron-hole excitations [40, 41]. A further reason for strong CDW damping may be the lack of CDW commensurability in the metallic phase of 1T-TaS₂. If the CDW distortion is incommensurate with the lattice, the frequency of the amplitude mode is not sharply defined, resulting in a faster dephasing of coherent oscillations in the time domain.

3.2. Dynamics and spectroscopy of the photoexcited insulator

In the following, we discuss the relaxation dynamics when the system is originally in the Mott phase ($T_1 = 30$ K). Figure 6(a) displays the time-resolved photoelectron intensity using

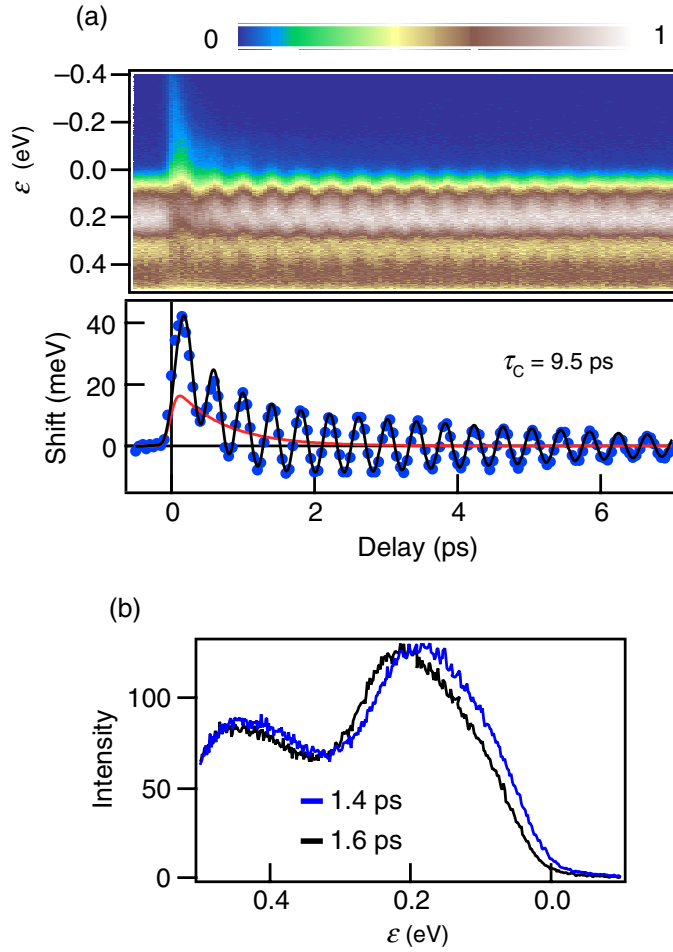


Figure 6. (a) Upper panel: intensity map of the photoelectron counts acquired in the insulating phase ($T_1 = 30$ K). Lower panel: time-dependent shift of the spectra as a function of pump–probe delay (blue marks). The initial response due e–e interaction (red line) plus the coherent oscillations of the CDW mode provide an excellent fit (black line) to the measured shift. (b) Two spectra acquired on a maximum ($\tau = 1.4$ ps) and minimum ($\tau = 1.6$ ps) of one CDW oscillation period display a rigid shift with respect to each other.

a false colorscale. Notice that large oscillations of $A_H(\epsilon, \tau)$ endure many picoseconds. In analogy to the metallic phase, such modulations are due to the ultrafast excitation of the CDW amplitude mode. As shown by figure 6(b), the coherent phonon induces a rigid shift of the entire spectral function. Although bulk and surface properties are very similar [31], we track some difference in the temporal evolution of the electronic spectra [18]. Therefore, we assume that surface and bulk contribution to the photoelectron counts are weighted by the positive factors c_S and $c_B = 1 - c_S$, respectively. We model the temporal shift of the photoelectron spectrum by a fitting function $E(\tau) + g c_S X_S(\tau) + g c_B X_B(\tau)$. The coordinate X_S and X_B stand for the CDW amplitude of the surface layer and of the bulk, g is the e–ph coupling of the CDW mode and $E(\tau) = E_0 \theta(\tau) e^{-\tau/\tau_H}$ is a spectral shift due to the pump-induced change of e–e correlations. The latter is related to the photo-induced phase transition of the Mott insulator

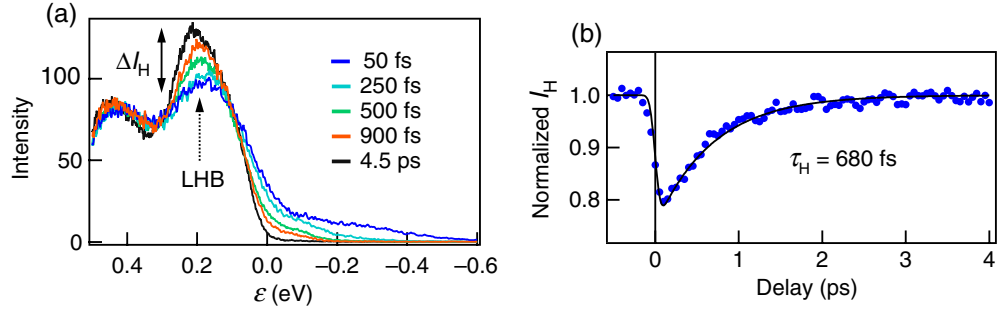


Figure 7. (a) Photoelectron spectra of the photoexcited insulator acquired at several pump–probe delays. The spectrum acquired before the arrival of the pump pulse is identical to the spectrum acquired at $\tau = 4.5$ ps. (b) Intensity of the LHB as a function of pump–probe delay (marks) and single exponential decay with time constant $\tau_H = 680$ fs (line).

and has no analog in the metallic phase. The temporal evolution of $X_{S,B}$ is calculated from equation (3) with oscillation frequencies $\nu_{S,B}$, damping time τ_C and force time τ_F . Figure 6(a) shows the convoluted result calculated for $\nu_S = 2.45$ THz, $\nu_B = 2.51$ THz, $c_S = 2c_B$, $\tau_C = 9.5$ ps, $\tau_F = 250$ fs and $\tau_H = 680$ fs. The frequency $\nu_B = 2.45$ THz is in perfect agreement with transient reflectivity [39, 42] and is therefore identified with the bulk CDW displacement. Conversely the frequency $\nu_S = 2.51$ THz is attributed to the surface CDW displacement. A stiffer and stronger CDW at the surface of 1T-TaS₂ is expected because of the lower coordination of the sulfur atoms. Phase space arguments account for the weak damping of the CDW oscillations in the MI phase: due to the Pauli exclusion principle and energy conservation, the CDW mode could decay only in final electronic states with excitation energy $|\epsilon| \simeq h\nu_{S,B} \simeq 10$ meV. However, the MI gap $\Delta \simeq 0.1$ eV precludes the existence of electronic excitations with $|\epsilon| < \Delta$. Therefore, the only anharmonic decay of the CDW amplitude mode in other phonon modes is the available damping mechanism. This decay channel originates from ph–ph interaction and has a timescale of several picoseconds [40, 41].

If the Mott insulator is in equilibrium at $T_e = T_l = 30$ K, the spectral function displays a LHB at $\epsilon = 0.21$ eV and vanishing density of electronic states at the Fermi level. Just after photoexcitation, the energy density deposited in the electronic system is too large for the existence of a Mott insulator. Figure 7(a) shows the photo-induced transfer of spectral weight from the LHB to the Fermi level. The electronic gap is partially filled by transient electronic states and recovers along with the energy relaxation of the hot electrons. Such midgap states must have very weak coupling to the CDW mode, otherwise they would lead to efficient damping of the CDW oscillations. The LHB intensity I_H in figure 7(b) is an empirical measure for the transfer of spectral weight toward the pseudogap. The instantaneous decrease and subsequent recovery of I_H can be described by an exponential decay $1 - I_0\theta(\tau)e^{-\tau/\tau_H}$ with time constant $\tau_H = 680$ fs. It follows that the MI gap collapses on a timescale much shorter than the pump–probe cross-correlation and monotonically recovers with subpicosecond timescale. This finding is consistent with the revival of a MI groundstate whereas it is *not* consistent with the dynamics of a Peierls insulator. If the electronic gap originated from the CDW amplitude mode, the recovery of I_H would follow the oscillatory behavior of the spectral shift in figure 6(a) and not the monotonic evolution of figure 7(b). Secondly, a Peierls gap would collapse after the

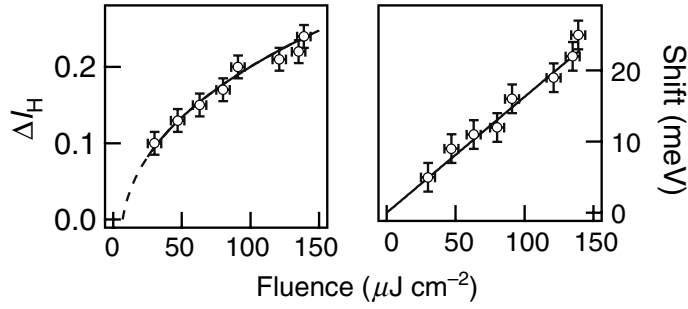


Figure 8. (a) Relative change of LHB intensity measured at 50 fs as a function of the pump fluence. (b) Relative shift between a spectra acquired at $\tau = 1.4$ and $\tau = 1.6$ ps as a function of the pump fluence.

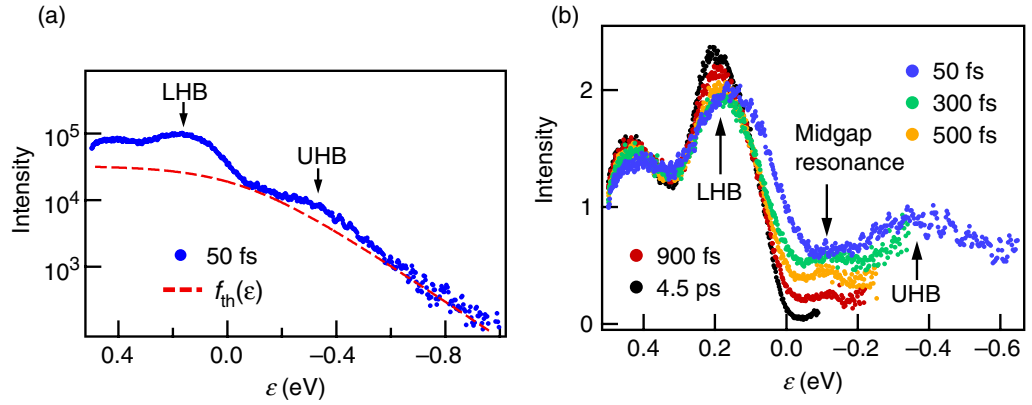


Figure 9. (a) Photoelectron spectrum acquired in the MI phase ($T_1 = 30$ K) for $\tau = 50$ fs (dots) and Fermi-Dirac distribution calculated for $\mu = -50$ meV and $T_e = 1800$ K (red dashed line). (b) Photoelectron spectra acquired at several pump-probe delays have been divided by the respective distribution functions. At $\tau = 50, 300, 500, 900$ and 4 ps, the electronic distribution is a Fermi-Dirac distribution with $T_e = 1800$ K $T_e = 900, 760, 570$ and 60 K, respectively. The LHB, UHB and the midgap resonance have been marked by arrows.

CDW mode reaches the maximum of the coherent amplitude. Figure 5 shows that such delay time would be $\tau = 1/4\nu \simeq 100$ fs but the decrease of I_H in figure 7(b) displays no sign of such retardation. Finally, the photoinduced displacement of the CDW and the relative change of the LHB intensity increase differently with the fluence of the pump beam: figures 8(a) and (b) compare the amplitude of the spectral oscillations with the reduction of peak intensity ΔI_H for varying pump fluence. Notice that the amplitude of the spectral shift increases linearly in the entire range of fluence whereas ΔI_H does not.

An inspection of the photoelectron spectra on a semilogarithmic scale provides further insights on the electronic properties of the photoexcited insulator. The broad feature above the Fermi level at $\epsilon = -0.35$ eV in figure 9(a) has no counterpart in the spectrum of the metallic phase (see figure 4(a)). We attribute this structure to the UHB of the Mott insulator. Its energy position is similar to the value reported by STS [22]. This agreement is somehow surprising, since the spectrum of figure 9(a) refers to a highly excited state. In spite of the high-excitation

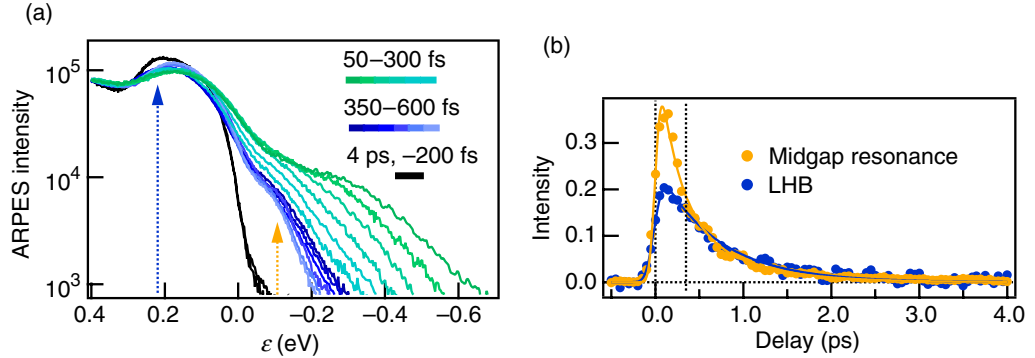


Figure 10. (a) Semilogarithmic plot of ARPES spectra acquired in the photoexcited insulator ($T_i = 30$ K) at several pump–probe delays. Spectra with $50 \text{ fs} < \tau < 300 \text{ fs}$ (lines from green to turquoise) display rapid cooling whereas spectra with $\tau > 300 \text{ fs}$ (lines from blue to azure) are slowly changing. The spectrum relative to 4.5 ps and the spectrum acquired before the absorption of the pump-pulse are almost identical (black line). Blue and yellow arrows mark the energy position of the LHB and midgap resonance, respectively. (b) Photo-induced change of the photoelectron counts at the midgap resonance (yellow marks) and at the LHB (blue marks). The photoelectron intensity at the midgap resonance has been rescaled in order to match ΔI_H for $\tau > 300 \text{ fs}$.

density, the Hubbard bands do not merge into a unique spectral feature. They are expected to collapse at even higher pump fluences, but it is impossible to reach such a regime without destroying the long range order of the CDW (irreversible sample damage).

An exact retrieval of the spectral function would require the knowledge of the electronic distribution [43]. Since a direct measurement of the isolated f is not possible, we rely on the small $f/f_{\text{th}} - 1$ observed in the metallic phase (see figure 4(b)) and assume in the following discussion nearly thermalized electrons also for the photoexcited insulator. Figure 9(b) displays the spectral function extracted from the ratio between the measured spectrum $A_H \cdot f$ and a Fermi–Dirac distribution f_{th} . We find that the chemical potential is pinned at the edge of the LHB for $T_e = 30$ K, probably due to a minor amount of acceptor dopants. However, at excitation densities of 0.1 electrons per reconstructed unit cell the effects of these impurities becomes negligible and the chemical potential is identified with the nominal center of the MI gap ($\mu = \Delta/2 = -50 \text{ meV}$). Notice that the midgap states connecting LHB and UHB display a small peak at $\epsilon \simeq -0.1 \text{ eV}$ for delays $\tau > 300 \text{ fs}$. This resonance suggests the existence of renormalized electronic states in proximity to the chemical potential. In the framework of the Fermi liquid theory, such renormalized electronic states should be quasiparticles with an effective mass larger than the bare band mass. Further investigations as a function of the photoelectron wavevector are necessary in order to find out whether the energy of this resonance shows any dispersion.

Next, we show that the dynamics of the photoexcited insulator is qualitatively different from that of the metallic phase: as shown by figure 10(a), the electronic occupation of states above the chemical potential decays faster for $\tau < 300 \text{ fs}$ and slower at larger pump–probe delays. We track this temporal evolution by plotting in figure 10(b) the photoelectron counts at the midgap resonance. The build-up of photoelectron intensity $A_H(\epsilon, \tau) \cdot f(\epsilon, \tau)$ at the energy

of the midgap resonance $\epsilon = -0.1$ eV is described by an instantaneous process convoluted by the pump–probe cross-correlation. The subsequent relaxation follows a double exponential decay with time constants $\tau_e = 200$ fs and $\tau_H = 680$ fs. Since $A_H(\epsilon, \tau)$ is fairly similar for $\tau = 50$ fs and $\tau = 300$ fs (see figure 9(b)), we conclude that the initial decrease of midgap intensity reflects the decay of the electronic distribution. However, after 300 fs the temporal evolution of f reaches a bottleneck, and the reduction of midgap intensity follows the intrinsic recovery of the MI gap. Accordingly, the photoinduced change of photoelectron intensity at the midgap resonance ($\epsilon \simeq -0.1$ eV) and at the LHB ($\epsilon \simeq 0.2$ eV) merge into a unique curve for delay times $\tau > 300$ fs. We propose two different explanations to account for the anomalous relaxation of the photoexcited insulator: (i) the average e–ph coupling of the midgap states strongly depends on the excitation density. It is largest just after absorption of the pump pulse and progressively reduces with τ . (ii) A small subset of phonon modes exhibit an e–ph coupling which is higher than the average value. The hot electrons thus generate non-equilibrium phonons on a timescale $\tau_e = 200$ fs. Afterwards, the e–ph interaction with weakly coupled mode and the ph–ph decay of non equilibrium phonons determine the cooling time $\tau_H = 680$ fs. A similar bottleneck of electronic energy has been already observed in anisotropic compounds such as graphite [44] or $\text{Bi}_2\text{Sr}_2\text{CaCu}_2\text{O}_{8+\delta}$ [45].

4. Theoretical modeling

This section introduces the simplest theoretical model accounting for CDW oscillations and the photoinduced collapse of the MI gap. The Hamiltonian $H = H_{e-e} + H_{e-ph}$ consists of a purely electronic H_{e-e} plus the coupling H_{e-ph} to the CDW mode. All other phonon modes are treated as a thermal bath leading to the energy relaxation of photoexcited electrons. We neglect the quantum nature of the phonon field because the CDW motion is much slower than the electronic motion. In the adiabatic limit the e–ph interaction is

$$H_{e-ph} = gX \sum_{i,\sigma} n_{i,\sigma}, \quad (4)$$

where $n_{i,\sigma}$ is the occupation of site i and spin σ , the parameter g stands for the e–ph coupling and X is the phonon coordinate calculated from equation (3). The coordinate X does not depend on site i because the ultrafast generation mechanism sets a unique starting time of nuclear motion in all crystal cells. It follows that H_{e-ph} changes only the total energy of the electronic system. Under this condition, the CDW interaction results in a rigid shift $A_H(\epsilon - gX)$ of the H_{e-e} spectral function $A_H(\epsilon)$. This result is experimentally verified by the spectra of figure 6(b).

At early pump–probe delays, the high-electronic temperature T_e induces an ultrafast crossover from the MI phase to the high-temperature region in figure 1. We simulate the experimental spectra by the one band Hubbard model

$$H_{e-e} = -t \sum_{\langle i,j \rangle, \sigma} (c_{i,\sigma}^\dagger c_{j,\sigma} + c_{j,\sigma}^\dagger c_{i,\sigma}) + U \sum_i n_{i,\uparrow} n_{i,\downarrow} \quad (5)$$

with Coulomb repulsion $U = 0.5$ eV, bandwidth $W = 0.36$ eV and filling of $n_\uparrow = n_\downarrow = 0.48$ electrons per unit cell. Figure 11(a) and (b) show the spectral function calculated by the dynamical mean field theory (DMFT) at the center of the Brillouin zone for different electronic temperatures $50 \text{ K} < T_e < 2500 \text{ K}$. The evolution of $A_H(\epsilon, T_e)$ defines different temperature

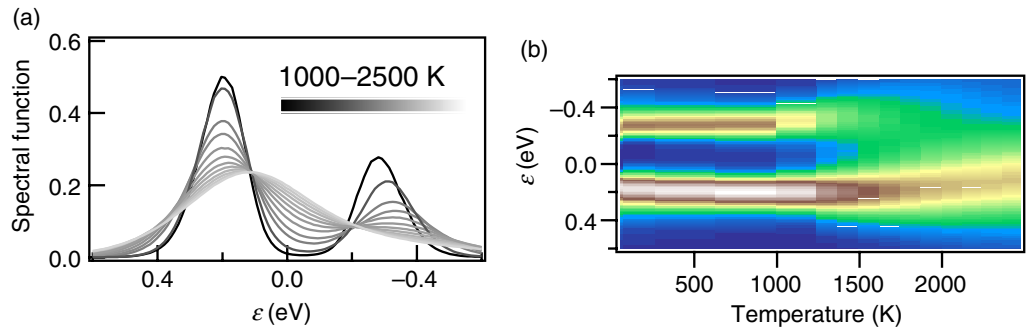


Figure 11. (a) Spectral function calculated at the center of the Brillouin zone for several temperatures between 1000 and 2500 K (lines from black to gray). (b) Theoretical map of the spectral function as a function of binding energy and electronic temperature.

windows: below $T_e = 1000$ K, the spectral function consists of the Hubbard bands separated by an electronic gap $\Delta \simeq 0.15$ eV. Above 1000 K, the gap is gradually filled by low energy excitations. For electronic temperatures higher than 1800 K, the LHB and UHB merge into a unique feature. The agreement with the MI collapse observed in figure 9(b) is fairly good. However, some relevant aspects distinguish the theoretical predictions from the experimental results. The crossover region predicted by the single band Hubbard model is a nascent metal in which quasiparticles are not yet formed. As shown by figure 11(a), the calculated midgap states have no sharp structure near to the chemical potential. Conversely, the experimental midgap resonance shown in figure 9(b) is similar to the quasiparticle peak observed in the symmetrized spectra of the metallic phase [6, 23]. In addition, the DMFT calculations of figure 11(b) predict an abrupt collapse of the MI gap at electronic temperatures $T_e \simeq 1200$ K. In contrast, the experimental midgap states develop already for $T_e > 600$ K and increase gradually up to the highest electronic temperature. This discrepancy may require extensions of the theoretical model taking into account effects involving more than one band or could be due to the spatial fluctuations of the electronic system, which could be important in a quasi-two-dimensional compound such as 1T-TaS₂ but are neglected by DMFT calculations [3].

5. Conclusions

We have performed time-resolved photoemission studies on the MI phase and metallic phase of 1T-TaS₂. The dynamics of the electronic states strongly depend on the initial phase of the system. We always observe periodic oscillations of the photoelectron spectra that are due to the ultrafast excitation of the CDW mode. However, the oscillations of electronic states decay 10 times faster in the metallic phase than in the insulating one. Upon photoexcitation of the insulating phase, we observed the quasi-instantaneous collapse of the electronic gap and its subsequent recovery on a subpicosecond timescale. A comparison of such dynamics with the coherent oscillation of the CDW proves that 1T-TaS₂ is a Mott insulator instead of a Peierls insulator. The spectra of the photoexcited insulator displays a clear signature of the Hubbard bands and suggest the presence of midgap quasiparticles. Theoretical calculations based on the single band Hubbard model results in a spectral function that correctly reproduces the evolution of the Hubbard bands.

Acknowledgments

We thank M Grioni and P S Kirchmann for fruitful discussions. This work has been supported by the Deutsche Forschungsgemeinschaft, a Marie Curie Fellowship (Contract No. 514954), the French ANR under project ETSF and a grant of computer time at IDRIS Orsay under project number 071393.

References

- [1] Mott N F and Peierls R 1937 *Proc. Phys. Soc. Lond. A* **49** 72
- [2] Imada M, Fujimori A and Tokura Y 1998 *Rev. Mod. Phys.* **70** 1039
- [3] Georges A *et al* 1996 *Rev. Mod. Phys.* **68** 13
- [4] Varma C M *et al* 1983 *Phys. Rev. Lett.* **68** 138
- [5] Fazekas P and Tosatti E 1979 *Phil. Mag. B* **39** 229
- [6] Perfetti L *et al* 2003 *Phys. Rev. Lett.* **90** 166401
- [7] Colonna S *et al* 2005 *Phys. Rev. Lett.* **94** 036405
- [8] Allen P B 1987 *Phys. Rev. Lett.* **59** 1460
- [9] Merlin R 1997 *Solid State Commun.* **102** 207
- [10] Rini M *et al* 2007 *Nature* **449** 72
- [11] Chollet M. *et al* 2005 *Science* **307** 86
- [12] Cavalleri A *et al* 2004 *Phys. Rev. B* **70** 161102
- [13] Iwai S *et al* 2003 *Phys. Rev. Lett.* **91** 057401
- [14] Kübler C 2007 *Phys. Rev. Lett.* **99** 116401
- [15] Haight R *et al* 1985 *Phys. Rev. Lett.* **54** 1302
- [16] Lisowski M *et al* 2004 *Appl. Phys. A* **78** 165
- [17] Rhie H S, Dürr H A and Eberhardt W 2003 *Phys. Rev. Lett.* **90** 247201
- [18] Perfetti L *et al* 2006 *Phys. Rev. Lett.* **97** 067402
- [19] Dardel B *et al* 1992 *Phys. Rev. B* **45** 1462
- [20] Harper J M E *et al* 1977 *Phys. Rev. B* **15** 2943
- [21] Yamamoto A 1983 *Phys. Rev. B* **27** 7823
- [22] Kim J-J *et al* 1994 *Phys. Rev. Lett.* **73** 2103
- [23] Perfetti L *et al* 2005 *Phys. Rev. B* **71** 153101
- [24] Clerc F *et al* 2006 *Phys. Rev. B* **74** 155114
- [25] Rossnagel K and Smith N V 2006 *Phys. Rev. B* **73** 073106
- [26] Di Salvo F J *et al* 1975 *Phys. Rev. B* **12** 2220
- [27] Dardel B *et al* 1992 *Phys. Rev. B* **45** 1462
- [28] Barker A S *et al* 1975 *Phys. Rev. B* **12** 2049
- [29] Gasparov L V *et al* 2002 *Phys. Rev. B* **66** 094301
- [30] Tani T *et al* 1977 *Solid State Commun.* **22** 269
- [31] Burk B *et al* 1992 *Science* **257** 362
- [32] Smith N V *et al* 1993 *Phys. Rev. B* **47** 15476
- [33] Wagner M 1991 *Phys. Rev. B* **44** 6104
- [34] Nessler W *et al* 1998 *Phys. Rev. Lett.* **81** 4480
- [35] Koralek J D *et al* 2006 *Phys. Rev. Lett.* **96** 017005
- [36] Hertel T and Moos G 1999 *Phys. Rev. Lett.* **84** 5002
- [37] Murray É D *et al* 2007 *Phys. Rev. B* **75** 184301
- [38] Sugai S *et al* 1985 *Phys. Status Solidi b* **129** 13
- [39] Demsar J *et al* 2002 *Phys. Rev. B* **66** 041101
- [40] Ishioka K *et al* 2008 *Phys. Rev. B* **77** 121402

- [41] Hase M *et al* 2002 *Phys. Rev. Lett.* **88** 067401
- [42] Toda Y *et al* 2004 *Phys. Rev. B* **70** 033106
- [43] Lisowski M *et al* 2005 *Phys. Rev. Lett.* **95** 137402
- [44] Kampfrath T *et al* 2005 *Phys. Rev. Lett.* **95** 187403
- [45] Perfetti L *et al* 2007 *Phys. Rev. Lett.* **99** 197001